The bionic sunflower: a bio-inspired autonomous light tracking photocatalytic system

Jingjing Qin,[a] Kaibin Chu,[a] Yunpeng Huang,[a] Xiangmiao Zhu,[a] Johan Hofkens,[bc] Guanjie He,[d] Ivan P. Parkin,[d] Feili Lai*[b] and Tianxi Liu*[a]

[a] The Key Laboratory of Synthetic and Biological Colloids, Ministry of Education, School of Chemical and Material Engineering, International Joint Research Laboratory for Nano Energy Composites, Jiangnan University, Wuxi 214122, P. R. China.
E-mail: txliu@jiangnan.edu.cn

[b] Department of Chemistry, KU Leuven, Celestijnenlaan 200F, Leuven 3001, Belgium.
E-mail: feili.lai@kuleuven.be

[c] Max Planck Institute for Polymer Research, Ackermannweg 10, Mainz 55128, Germany

[d] Christopher Ingold Laboratory, Department of Chemistry, University College London, 20 Gordon Street, London WC1H 0AJ (UK)

Broader context

Phototropism is considered to be an effective means for natural organisms to maximize light energy harvesting. Artificial phototropism provides a great possibility to make full use of light energy. Photocatalysis based on sunlight as a source of energy is an alluring choice due to its possibility of purification of different contaminants. However, the traditional photocatalytic technology requires direct irradiation using a fixed light source and lacks the ability to collect light autonomously, which greatly reduces light utilization. Therefore, it is of great significance to develop a novel photocatalytic reactor that can capture light energy independently and efficiently. Here, inspired by sunflowers, we prepared a bionic sunflower based on phototropic smart hydrogels. It can automatically track the direction of light at any incident angle from 0 to

90° to recover the oblique-incidence energy-density loss (E) and perform photocatalytic reactions. Compared with the control sample, the photocatalytic efficiency of the bionic sunflower is always maintained at a relatively stable and high level under 0-90° irradiation. This general strategy provides a new photocatalytic system for efficiently using solar energy.

Abstract

Developing a self-adapting photocatalytic system that efficiently captures light all day is not only a dream but also a challenge. Here, we report a 'bionic sunflower' based on a light-responsive smart hydrogel, which can spontaneously track and orient itself directionally to a light source, mimicking phototropism in, e.g., plants. As a novel photocatalytic system, it can efficiently recover the oblique-incidence energy-density loss and maintain photocatalytic efficiency at the maximum level at any random incidence angle from 0 to 90°. By taking the photocatalysis of H_2O_2 generation as an example, the bionic sunflower displays a high H_2O_2 yield rate of 262.1 μmol g^{-1} h^{-1} under 90° irradiation, as compared with the same photocatalytic system without phototropism (83.5 μmol g^{-1} h^{-1}). Theoretical analyses with COMSOL Multiphysics simulation and density functional theory (DFT) calculations reveal the mechanism behind the actuation motion that triggers the bending of the bionic sunflower and determine the active sites for H_2O_2 generation during photocatalysis. This work proposes a novel photocatalytic concept to boost any traditional photocatalytic reaction by optimally using the solar energy from the sun's passage.

Introduction

Phototropism is the ability of a plant, or other photosynthesizing organisms, to grow directionally in response to a light source. This phenomenon is commonly found in many natural organisms (e.g., sunflower), and can empower the organisms to self-adapt to the changes in surrounding light and maximize energy harvesting.[1] By taking a sunflower as an archetype, phototropism allows it to recover oblique-incidence energy-density losses and to quickly increase the temperature of the floral disk, which facilitates plant growth and reproduction.[2] Therefore, phototropism can be regarded as an efficient strategy to ensure that the inclined plane of a system is largely perpendicular to the incident light, even when the angle of incident light

changes, compensating for energy-density (E) losses due to oblique irradiation.[3] Mathematically speaking, as shown in Fig. S1 (ESI†), the energy density received by the surface can be quantified through the following equation:[4]

$$E = E_{max} \cdot \cos\theta \tag{1}$$

where E, E_{max}, and θ represent the in-plane energy density received, the energy density received during vertical irradiation, and the zenith angle, respectively. Obviously, the energy loss increases with increasing oblique angle (e.g., only 50% energy received when $\theta = 60°$). Artificial systems equipped with phototropism, inspired by natural organisms, solve this challenge by constantly tracking sunlight.

Recently, artificial phototropism has been mainly applied in the fields of electromechanical devices and photo-responsive polymers, which are used for constructing multi-functional components or for following non-steady oscillatory irradiation directions.[4,5] However, it is still a challenge to build a material with artificial phototropism that is independent of an external control and that tracks moving light sources steadily, making it necessary to propose a new design.[6] We opted for using hydrogels to realize such a system. Hydrogels with excellent biocompatibility and chemical stability have attracted intensive attention due to their three-dimensional (3D) network and interconnected porous structures.[7-9] After years of development, hydrogels have evolved from a static material to a smart one, as they can show physical or chemical changes in response to an external stimulus (e.g., temperature, pH, light, electrical field, and magnetic field), making them widely used in the applications of sensors, actuators, wearable devices, and biomedicine.[10-18] As light is non-invasive and allows remote control, photo-responsive hydrogels have become highly attractive and have contributed greatly to bespoke applications.[19–21] Ever since the first discovery of thermal phase transition behavior in poly(N-isopropylacrylamide) (PNIPAAm), it has become one of the most studied materials in thermosensitive hydrogels.[22–24] Due to the low critical solution temperature (LCST, ~32 °C) of PNIPAAm in aqueous media, PNIPAAm-based smart hydrogels show drastic and reversible volume phase transitions through swelling/shrinking processes when the temperature approaches the LCST.[25] To construct photosensitive PNIPAAm-based intelligent hydrogels, there are three main strategies that can be considered: (i) shape deformations can be successfully realized in bilayer hydrogel structures with

differential swelling/shrinkage rates due to the asymmetric deformation of the two layers; (ii) polymer chains with a gradient distribution may lead to different swelling rates at different locations, resulting in shape changes; and (iii) polymers with specific structural features can react to local stimuli.[26–29] He et al. proposed a general principle for the realization of artificial light-orienting polymer materials.[3] By simulating biologically asymmetric growth, a negative feedback loop is formed within the hydrogel to achieve artificial phototropism through a reversible swelling/shrinkage deformation and photothermal conversion of the soft material.

However, photosensitive smart hydrogels have never been applied in photocatalytic reactors that are typically directly illuminated using a fixed light source and are short of the ability to collect light autonomously.[30-32] In practice, however, the oblique-incidence energy-density loss caused by the changes in the incidence of sunlight always exists and cannot be ignored. Therefore, it is of great significance to develop a new type of light-driven photocatalytic reactor that can track and capture light energy autonomously and efficiently.

In this work, inspired by the phototropism of sunflowers, we prepared a so-called bionic sunflower as a photocatalytic reactor, which can autonomously bend towards light to maximize energy-harvesting. The stem and floral disk of the bionic sunflower are simulated using a rGO-PNIPAAm hydrogel and a CdS/rGO-PNIPAAm hydrogel, respectively. By taking photocatalysis of H_2O_2 generation as an example, it is proven that this sunflower mimicking photocatalyst can effectively recover the loss of oblique incidence energy density when compared to traditional photocatalysts without phototropism. Indeed, the bionic sunflower displays a well maintained and constant photocatalytic efficiency at any incident angle from 0 to 90°. When the incident angle is 90°, the H_2O_2 generation rate of the bionic sunflower is as high as 262.1 $\mu mol\ g^{-1}\ h^{-1}$, which is more than three times that of the control sample (83.5 $\mu mol\ g^{-1}\ h^{-1}$). This new photocatalytic system is of great significance for improving the utilization of light.

Results and Discussion

Inspired by the phototropism of sunflowers (Fig. 1a), we successfully prepared an artificial bionic sunflower, where two types of hydrogels were used to simulate the stem and disk of a sunflower (Fig. S2, ESI†), respectively. Particularly, a phototropic hydrogel was used as a stem

to realize the light-tracking process of a sunflower, which was generated by evenly distributing reduced graphene oxide (rGO) as a photo-absorber into a poly(N-isopropylacrylamide) (PNIPAAm) hydrogel, referred to as a rGO-PNIPAAm hydrogel (RPH) hereafter. The phototropic behavior was achieved by the photothermal conversion through rGO and the temperature-sensitive properties of the PNIPAAm hydrogel. For the floral disk, a CdS/rGO composite was mixed in N-isopropylacrylamide to obtain the second and photocatalytic CdS/rGO-PNIPAAm hydrogel (denoted CPH), which was used as a photoreactor to conduct a series of photocatalytic reactions (e.g., H_2O_2 generation). The two hydrogels were linked together directly by UV polymerization of the prepolymers. When light is focused on one side of the RPH, it will bend and orient itself to the direction of the incident light. As a result, the CPH part orients vertically toward the light, ensuring maximum light absorption. A digital photograph of the fabricated bionic sunflower is displayed in Fig. 1b. To observe the morphologies of both the CPH and RPH, the freeze-drying method was employed to maintain their 3D interconnected network. As the scanning electron microscope (SEM) images in Fig. 1c and d show, the pore size of the CPH is approximately 10 μm with an evenly distributed CdS/rGO composite in the 3D hydrogel, which is beneficial for providing a high specific surface area for enhanced mass transferability. Similarly, the RPH displays abundant cylindrical pores with diameters of about 50 μm, which can not only facilitate the flow of water into/out of the hydrogel but are also crucial for the realization of phototropism. To prove the mechanical stability of the bionic sunflower during the photocatalytic process, its stress–strain curve was further characterized, see Fig. S3 (ESI†). The bionic sunflower has a high fracture strain of 21.1%, which indicates the stable connection between the CPH and RPH.

As the main component in the CPH for photocatalysis, the morphology and chemical features of the CdS/rGO composite were further determined using transmission electron microscopy (TEM), X-ray diffraction (XRD) and UV-visible (UV-vis) diffuse reflectance spectra. As the TEM image shown in Fig. 1e indicates, abundant spherical CdS nanoparticles with an average size of about 200 nm are dispersed in the rGO nanosheets. The rGO substrate can effectively prevent the aggregation of CdS nanoparticles (Fig. S4, ESI†) and create abundant boundaries between CdS nanoparticles and rGO nanosheets. The XRD pattern shown in Fig. 1f of the CdS/rGO composite exhibits five distinct diffraction peaks, where the peaks at 25.2°, 26.7°,
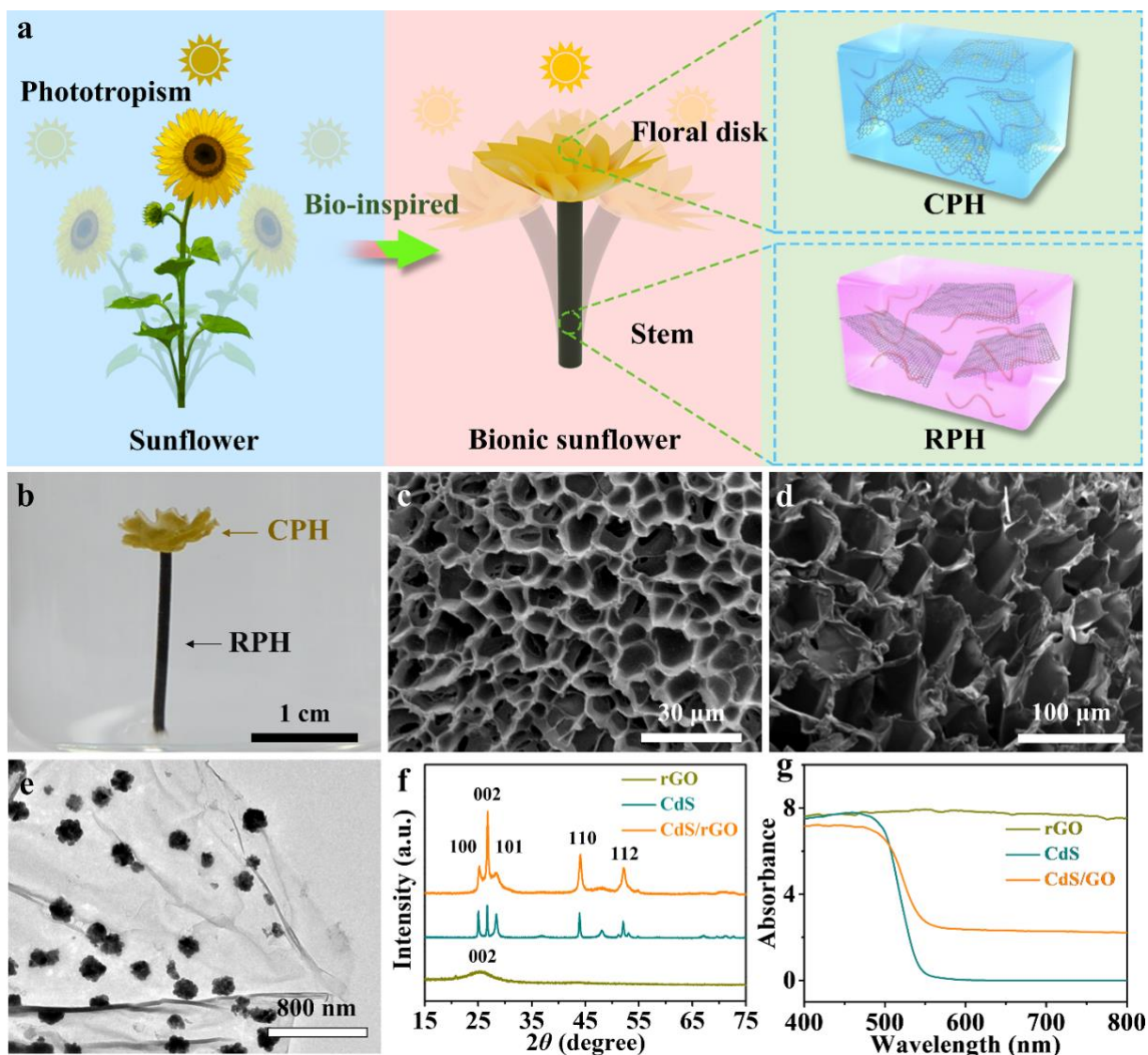
Fig. 1 (a) Schematic diagram of a natural sunflower and schematic illustration of the composition of the bionic sunflower. (b) A photograph of the as-fabricated bionic sunflower. SEM images of the (c) CPH and (d) RPH. (e)TEM image of CdS/rGO composite. (f) XRD patterns and (g) UV–Vis diffuse reflectance spectra of the rGO, CdS bulk, and CdS/rGO composite.

28.4°, 44.1° and 52.2° are assigned to the (100), (002), (101), (110) and (112) planes of the hexagonal phase for CdS (JCPDS: 41-1049).[33] The XRD pattern of the CdS/rGO composite is similar to that of the CdS bulk, which demonstrates that the incorporation of the rGO matrix does not affect the crystal structure of CdS. For the UV-vis spectra shown in Fig. 1g, the CdS bulk exhibits almost no light absorption above 500 nm, whereas the light absorption edge for the CdS/rGO composite positively shifts to about 570 nm due to the excellent visible-light

absorption of the rGO component. The band gap energies of the CdS bulk and CdS/rGO composite are calculated to be 2.36 eV and 2.29 eV (Fig. S5, ESI†), respectively. This difference originates from the positively shifted wavenumber for visible-light adsorption and the increased conductivity in the CdS/rGO composite, which make the electron transition much easier in CdS/rGO as compared with that in the CdS bulk. Additionally, the Raman spectra of the CdS bulk, rGO and CdS/rGO composite in Fig. S6 (ESI†) provide further evidence of the successful preparation of the CdS/rGO composite. Next, the structures of the PNIPAAm hydrogel (PH), RPH and CPH were characterized by XRD and FTIR. The XRD patterns shown in Fig. S7 (ESI†) show that the rGO component in the RPH does not affect the peaks of the PH at 7.8° and 20.4°. However, the peaks belonging to the CdS phase appear in the CPH, indicating the successful incorporation of CdS/rGO sheets in the whole 3D structure. The FTIR spectra in Fig. S8 (ESI†) provide information about the PH, RPH and CPH. The bands at 3289 and 2969 cm^{-1} represent N-H stretching and C-H stretching from PNIPAAm, respectively. The absorption bands at 1640 and 1539 cm^{-1} are characteristic of the -C=O stretch and N-H deformation from the PNIPAAm. In addition, to observe the distribution of rGO and CdS/rGO in the RPH and CPH, we performed energy dispersive X-ray (EDX) characterization (Fig. S9-S11, ESI†), and the results proved that they were uniformly distributed in the hydrogels. After calculating their contents separately, the results showed that CdS and rGO accounted for 77.1 wt% and 22.9 wt% in the CdS/rGO, and the contents of CdS and rGO in the CPH were 4.47 wt% and 1.33 wt%, respectively.

The light-responsive behavior of the bionic sunflower is shown in Fig. 2 and Movie 1 (ESI†). The bionic sunflower can track the incident light from 0° to 114° zenith angles at room temperature, demonstrating that the bionic sunflower maximizes the capture of light energy by orienting the CPH perpendicularly to the incident light. Interestingly, the shape of the bionic sunflower can return to its original state several minutes after turning off the light (Fig. 2b and Movie 2, ESI†). To record the shape stability and reversibility of this bionic sunflower, it was cycled 3 times under vertical light ($\theta = 90°$) illumination. The bionic sunflower finishes bending within 90 s and recovers in about 30 min after the light is turned off (Fig. S12, ESI†). As shown in Fig. 2c, the bionic sunflower still remains stable after three cycles of bending and recovery, which proves its good mechanical reversibility and stability. The driving force for the light-

responsive behavior of the bionic sunflower can be easily understood. Generally speaking, the
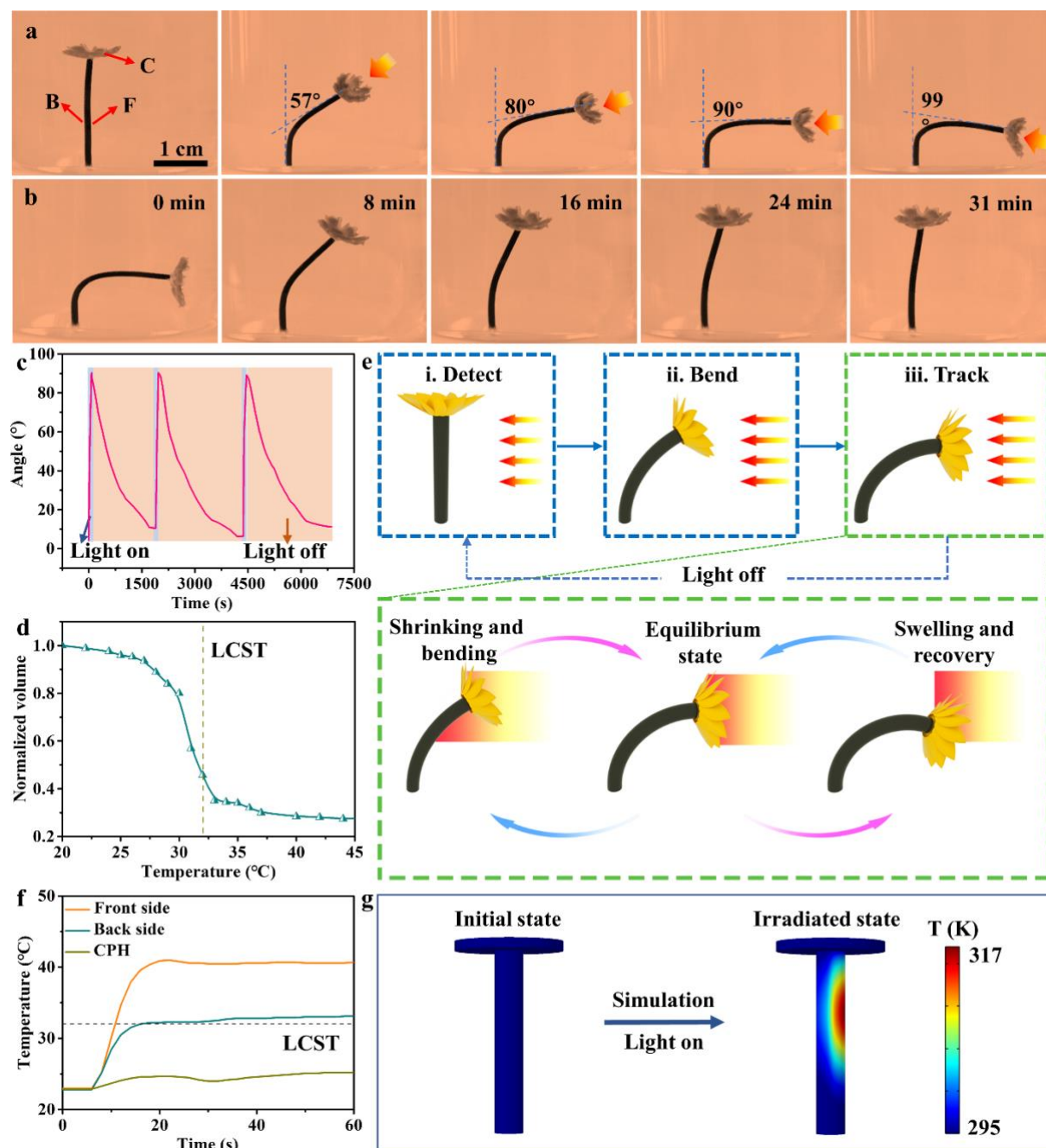
Fig. 2 (a) Photographs of a bionic sunflower at different angles of incident light. (b) Photographs for the shape recovery process of a bended bionic sunflower. (c) The shape stability for the light-responsive behavior of the bionic sunflower. (d) Normalized volume curve of the RPH with increasing temperature. (e) The as-proposed phototropic principle and process of the bionic sunflower. (f) The time-dependent temperatures at different sites of the bionic sunflower. (g) The simulated thermal distribution in the RPH model.
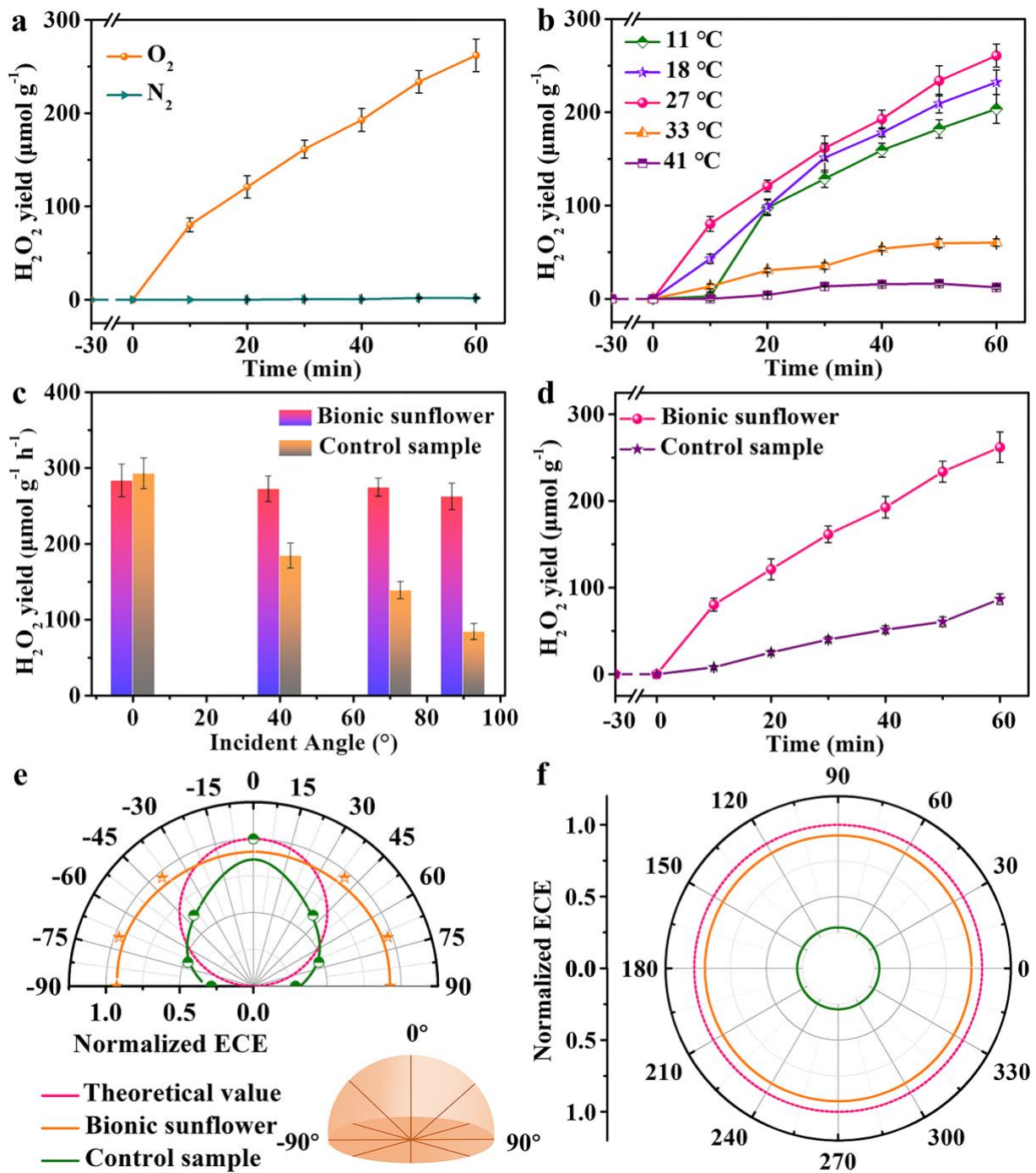
phototropism of the bionic sunflower is achieved by establishing a built-in negative feedback loop through the so-called self-shadowing effect in conjunction with reversible swelling/shrinkage typical for temperature sensitive hydrogels. PNIPAAm, used for both the CPH and RPH, has a low critical solution temperature (LCST, ~32 °C) in aqueous medium. When the system temperature is lower than the LCST, the polymer-solvent associations are stronger than polymer-polymer interactions. In this case, water is a good solvent for PNIPAAm with the generation of abundant hydrogen bonds, resulting in a volume expansion among the hydrophilic PNIPAAm chains. In comparison, the PNIPAAm chains turn into hydrophobic structures when the temperature is higher than the LCST. As a result, the water will be expelled from the PNIPAAm hydrogel as the polymer-solvent associations are dramatically replaced by polymer-polymer interactions, leading to the aggregation of the polymer network.[34] In order to check the LCST of PNIPAAm-based hydrogels, the RPH was taken as an example. As shown in Fig. 2d, the volume of the RPH decreases with increasing temperature and changes dramatically between 30 °C and 33 °C, which confirms that the LCST of the RPH is still fixed at around 32 °C. This implies that the incorporation of an additional component (e.g., rGO in the RPH) does not strongly affect the LCST of PNIPAAm.

Since the photothermal conversion material (rGO) is evenly dispersed in the temperature sensitive PNIPAAm, the energy from sunlight can be absorbed well and converted into heat. As shown in Fig. 2e (i and ii), upon illumination from one side of the bionic sunflower, the RPH undergoes one-sided shrinkage as its local temperature is above the LCST, whereas the temperature on the backside still stays below the LCST. Therefore, the hydrogel can bend due to asymmetric deformation. When the floral disk points toward the light, the actuation motion is terminated spontaneously because the disk on the top of the pillar blocks the light and stops the heating process on the illuminated side (self shadowing). Tracking is a dynamic process resulting from the interplay between light stimulation and its feedback loop. From state i to state ii, the bionic sunflower bends under irradiation, and may show a tendency to overbend as the temperature increases. At this point, the self-shadowing effect due to the disk allows the irradiated site on the stem to cool down and reach a dynamic equilibrium of state iii. After turning off the light, this equilibrium shifts, leading to the shape recovery of the bionic sunflower (state i). In order to monitor the temperature change of the hydrogel during

illumination, we placed three thermocouples: one on the frontside (F) of the RPH, one on the backside (B) of the RPH, and one on the surface of the CPH (C), as marked in Fig. 2a. As shown in Fig. 2f, the temperature at site F increases to 40 °C rapidly within 11 s, while the temperature at site B increases slowly and remains at the LCST (~32 °C). Similarly, the temperature distribution of the bionic sunflower is directly obtained using an infrared imaging camera with the initial and irradiated states shown in Fig. S13 (ESI†), where the temperature at the point of irradiation increases from 20.1 to 38.2 °C. This result provides strong evidence for the observed light-responsive behavior and proposed mechanism. Next, the swelling/shrinking rates of the RPH were evaluated at different temperatures (see Fig. S14 and S15, ESI†), from which it can be deduced that the RPH can reach equilibrium in 50 s during the shrinking process, and takes 30 min during the swelling process, demonstrating the good reversibility of the RPH. Furthermore, the time-variant thermal distribution in the RPH was simulated using the COMSOL Multiphysics simulation package, where the thermal distributions of the initial state and irradiated state were recorded by the transient thermal analysis method with relevant parameters of the hydrogel shown in Table S1 (ESI†). As demonstrated by the simulation results shown in Fig. 2g and Fig. S16 and Movie 3 (ESI†), the temperature on the frontside F of the RPH increases rapidly, while its backside B remains at a relatively lower temperature. This provides a theoretical confirmation for the light-responsive behavior of the bionic sunflower.

Subsequently, the bionic sunflower was applied as a photocatalytic reactor, where the CdS/rGO composite mixed into the CPH was regarded as the main photocatalyst for H_2O_2 generation (under various atmospheres, such as O_2 and N_2). During the test, six bionic sunflowers were completely immersed in 100 mL of water and illuminated vertically using a 300 W xenon lamp, and the concentration of H_2O_2 was measured by the colorimetric method (Fig. S17, ESI†). To ensure the consistency of the experiment, we fixed the distance between the reactor and the light source at 12 cm for all measurements. As shown in Fig. 3a, the photocatalytic system of the bionic sunflower only works to generate H_2O_2 under the O_2 atmosphere, not under the N_2 atmosphere. This demonstrates that the as-produced H_2O_2 molecules mainly come from the reduction of O_2 rather than the oxidation of H_2O. In detail, the maximum rate for H_2O_2 generation of the bionic sunflower under the O_2 atmosphere reaches

Fig. 3 H$_2$O$_2$ generation of the bionic sunflower (a) under different atmospheres and (b) at different temperatures. (c) H$_2$O$_2$ evolution rates of the bionic sunflower and a control sample without phototropism at different incident angles. (d) Dependence of H$_2$O$_2$ formation on time of the bionic sunflower and the control sample without phototropism under 90° irradiation. (e and f) Normalized ECEs (energy collection efficiencies) of the bionic sunflower and control sample at different zenith angles and azimuth angles (90° zenith angle). Experimental conditions: six bionic sunflowers were placed in 100 mL of water with O$_2$ purging under 300

W xenon lamp irradiation. Among them, the addition amounts of CdS/rGO and rGO in the CPH and RPH were 3% and 0.35%, respectively.

260.8 $\mu mol\ g^{-1}\ h^{-1}$ at 27 °C. The yields of H_2O_2 at different temperatures (from 11 to 41 °C) are also recorded in Fig. 3b, from which the optimal temperature for H_2O_2 generation can be fixed at around 27 °C. On the other hand, when the reaction temperature is higher than 27 °C, the dramatically decreased H_2O_2 generation rate mainly originates from: (1) the decomposition of H_2O_2 at a higher temperature and (2) the reduced space to store enough O_2 molecules in the hydrogel after its shape shrinkage. Furthermore, we conducted a control experiment to confirm the positive effect of the light-responsive behavior of the bionic sunflower on its photocatalytic activity, where a control sample without phototropism was realized by physically fixing the RPH part with a rigid pillar (Fig. S18, ESI†). The photocatalytic results in Fig. 3c demonstrate that the light-responsive behavior of the bionic sunflower can definitely increase the H_2O_2 generation at any incident angle (> 0°). In particular, the rate of H_2O_2 generation for the control sample decreases dramatically, from 292.6 to 83.5 $\mu mol\ g^{-1}\ h^{-1}$, when the incident angle increases from 0° to 90°. However, the rate of H_2O_2 generation for the bionic sunflower always remains at a relatively stable and high level. Fig. 3d shows the H_2O_2 production in 60 min photoreaction under 90° irradiation, which also displays three times higher H_2O_2 generation in the bionic sunflower and demonstrates its excellent stability for practical application. These results indicate that the photocatalytic system of the bionic sunflower can not only track light autonomously, but also utilize the sunlight energy efficiently. Additionally, we found that the power of the light source has a strong effect on the rate of H_2O_2 production as shown in Fig. S19 (ESI†), where the yield of H_2O_2 decreases with the reduction of the illumination power under 0° irradiation. In order to understand the energy collection efficiency at different zenith angles and azimuthal angles, the theoretical and practical energy collection efficiencies (ECE) were determined and are plotted in Fig. 3e and f. It can be seen that for the zenith angles from -90° to 90°, the normalized ECEs of the bionic sunflower are always close to 0.9, with good stability. However, the normalized ECE of the control sample is only about 29% when the zenith angle is 90°, demonstrating that the bionic sunflower can almost recover ~60% energy loss from the light source.

As the CdS/rGO composite is the real photocatalyst in the bionic sunflower, its photocatalytic mechanism for H_2O_2 generation is still unveiled. Therefore, density functional theory (DFT) calculation was performed by constructing three atomic models, including CdS/rGO, CdS, and rGO (Fig. S20, ESI†). Generally, hydrogen peroxide might be generated by reducing O_2 through two routes: one-step two-electron direct reduction route (eqn (2)) and a sequential single-electron two-step indirect reduction process (eqn (3) and (4)) during the photocatalytic process.

$$O_2 + 2e^- + 2H^+ \rightarrow H_2O_2 \tag{2}$$

$$O_2 + e^- \rightarrow \cdot O^{2-} \tag{3}$$

$$\cdot O^{2-} + 2H^+ + e^- \rightarrow H_2O_2 \tag{4}$$

According to previous reports in the literature, the two-electron one-step reduction route (eqn (2)) dominates the whole H_2O_2 production process, while it is accompanied by a sequential single-electron two-step reduction route.[35] In addition, H_2O_2 can also be generated by the oxidation of water on photo-generated holes (eqn (5) and (6)).

$$H_2O + h^+ \rightarrow H^+ + \cdot OH \tag{5}$$

$$2 \cdot OH \rightarrow H_2O_2 \tag{6}$$
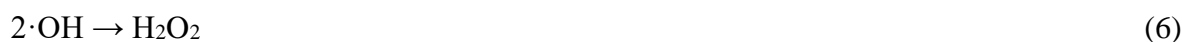
Notably there are two possible reaction sites existing in the CdS/rGO model, which are denoted as CdS/rGO-up (on the CdS side) and CdS/rGO-down (on the rGO side) as displayed in Fig. S20 (ESI†). Subsequently, the potential energy required for various steps, including the absorption of O_2/H_2O, the protonation/deprotonation process of the intermediates (*HOO/*OH) and the desorption of H_2O_2, were calculated and are shown in Fig. 4 and Table S2 (ESI†). For the two-electron oxygen reduction reaction (ORR) pathway (Fig. 4a), the CdS/rGO-up site presents the most negative adsorption energy toward O_2 molecules (-0.170 eV) among the four sites, indicating its strongest ability for the activation of O_2 molecules. Moreover, the desorption of H_2O_2 is the rate-determining step on the CdS/rGO-up site with an energy barrier of 0.127 eV, which is much lower than the values on the other three sites (CdS, CdS/rGO down, and rGO). All these results indicate that the CdS/rGO-up site is the best possible site for the ORR pathway. For the water oxidation reaction (WOR) pathway ($2H_2O + 2h^+ \rightarrow 2H^+ + H_2O_2$) in Fig. 4b, the CdS/rGO-up site also displays the most negative adsorption energy value towards the first step of water adsorption (*H_2O) as -0.419 eV among the four sites. Meanwhile, the rate-determining

step for the WOR pathway becomes the deprotonation process (*H_2O → *OH), which appears to have the lowest energy barrier of 2.364 eV on the CdS/rGO-up site. These calculation results demonstrate that the presence of rGO is conducive to the promotion of charge transfer and improvement of the reduction of O_2 and oxidation of H_2O, especially on the CdS/rGO-up site. It is to be noted that as the energy barrier for the ORR pathway is much lower than that of the WOR pathway, it indicates that the ORR pathway is the mainly conducted mechanism for H_2O_2 generation in our photocatalytic system.
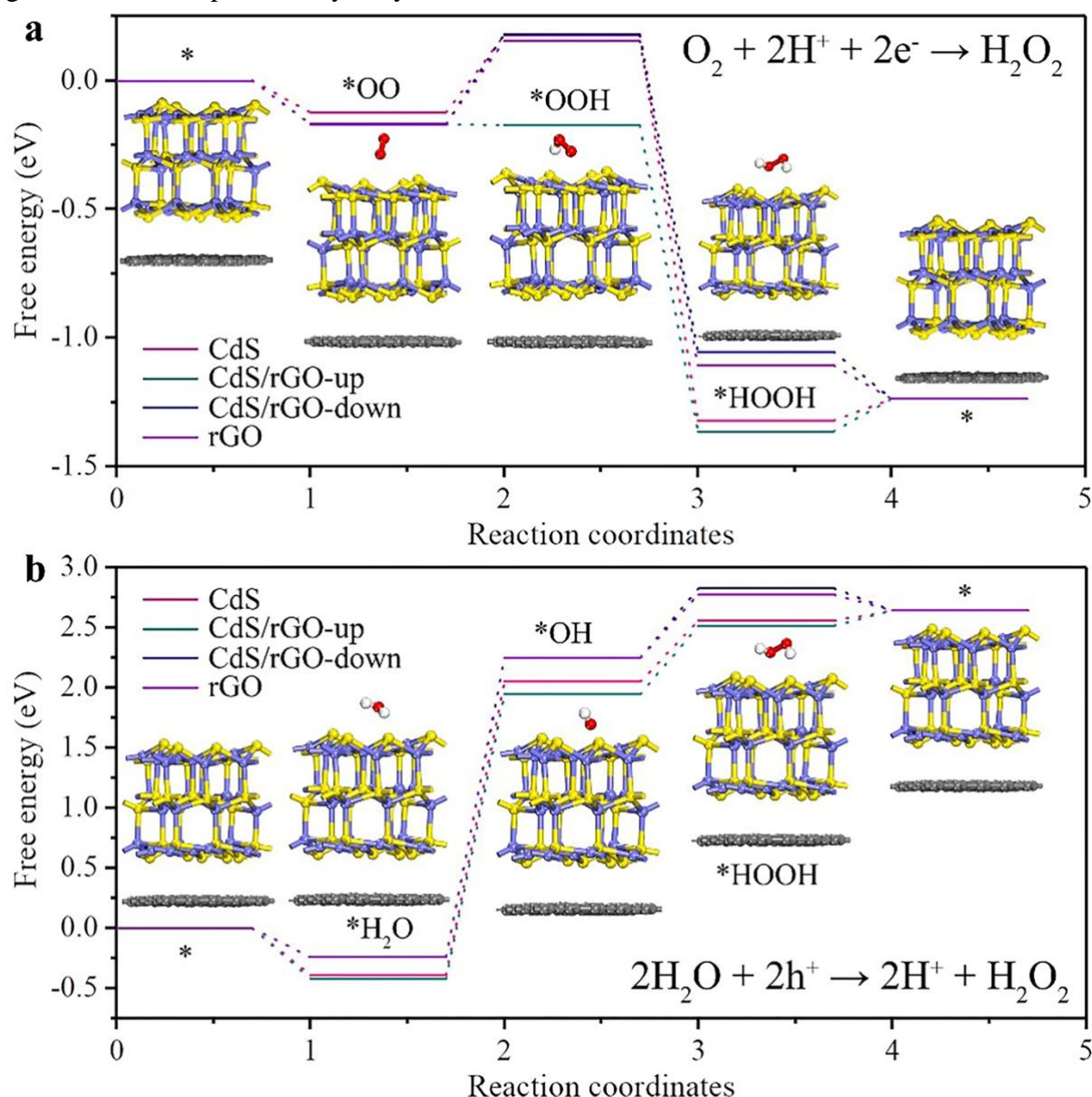
Fig. 4 (a and b) Free energy diagrams for H_2O_2 generation following two kinds of reaction mechanisms on different sites - CdS, CdS/rGO-up, CdS/rGO-down, and rGO. The insets show the optimized structures on the CdS/rGO-up surface during the catalytic process.

Conclusion

In summary, we have prepared a bionic sunflower to recover oblique incidence energy-density losses and maximize light energy-harvesting. The system is conceived such that the stem of the bionic sunflower displays phototropic behavior and quickly adapts to the direction of the light. This is achieved using a photo-responsive smart hydrogel prepared from a temperature-sensitive polymer, PNIPAAm. The disk on the top of the bionic sunflower contributes to the self-shadow function and contains the photocatalyst responsible for H_2O_2 generation. COMSOL Multiphysics simulations, as well as the corresponding experiments, confirm the existence of the bending force caused by a temperature difference in the stem of the bionic sunflower. The bionic sunflower can achieve a higher H_2O_2 yield rate of 262.1 μmol g^{-1} h^{-1} under 90° irradiation, as compared with a photocatalytic system without phototropism (83.5 μmol g^{-1} h^{-1}). Two different mechanisms for H_2O_2 generation were found on the surface of the CdS/rGO composite with the determination of real active sites. This paper reports a novel photocatalytic concept, demonstrated by boosting the efficiency of photocatalytic H_2O_2 generation, but can be extended to any traditional photocatalytic reaction by more efficiently using solar energy through artificial phototropism.

Conflicts of interest

The authors declare no conflict of interest.

Notes and references

1. G. Jékely, J. Colombelli, H. Hausen, K. Guy, E. Stelzer, F. Nédélec and D. Arendt, *Nature*, 2008, **456**, 395-399.
2. H. S. Atamian, N. M. Creux, E. A. Brown, E. A. Brown, A. G. Garner, B. K. Blackman and S. L. Harmer, *Science*, 2016, **353**, 587-590.
3. X. Qian, Y. Zhao, Y. Alsaid, X. Wang, M. Hua, T. Galy, H. Gopalakrishna, Y. Yang, J. Cui, N. Liu, M. Marszewski, L. Pilon, H. Jiang and X. He, *Nat. Nanotechnol.*, 2019, **14**, 1048-1055.
4. A. H. Gelebart, G. Vantomme, E. W. Meijer and D. J. Broer, *Adv. Mater.*, 2017, **29**, 1606712.
5. S. Seral, N. Tabityan, R. Vergara, T. J. White, R. A. Vaia and T. J. Bunning, *Soft Matter*, 2010, **6**, 779-783.
6. Y. Zhao, C. Xuan, X. Qian, Y. Alsaid, M. Hua, L. Jin and X. He, *Sci. Robot.* 2019, **4**, eaax7112.
7. C. Ma, Y. Shi, D. A. Pena, L. Peng and G. Yu, *Angew. Chem., Int. Ed.*, 2015, **54**, 7376-7380 (*Angew, Chem.*, 2015, **127**, 7484-7488).
8. A. Jayakumar, V. K. Jose and J.-M. Lee, *Small Methods*, 2020, **4**, 1900735.
9. Z.-X. Zhang, K. L. Liu and J. Li, *Angew. Chem., Int. Ed.*, 2013, **52**, 6180-6184 (*Angew. Chem.*, 2013, **125**, 6300-6304).
10. E. S. Gil and S. M. Hudson, *Prog. Polym. Sci.*, 2004, **29**, 1173-1222.
11. T. Kureha, D. Aoki, S. Hiroshige, K. Iijima, D. Aoki, T. Takata and D. Suzuki, *Angew. Chem., Int. Ed.*, 2017, **56**, 15393-15396 (*Angew. Chem.*, 2017, **129**, 15595-15598).
12. G. Pan, Q. Guo, Y. Ma, H. Yang and B. Li, *Angew. Chem., Int. Ed.,* 2013, **52**, 6907-6911 (*Angew. Chem.*, 2013, **125**, 7045-7049).
13. Z. Sun, Y. Yamauchi, F. Araoka, Y. S. Kim, J. Bergueiro, Y. Ishida, Y. Ebina, T. Sasaki, T. Hikima and T. Aida, *Angew. Chem., Int. Ed.*, 2018, **57**, 15772-15776 (*Angew. Chem.*, 2021, **60**, 23348-23349).
14. J. Gacanin, J. Hedrich, S. Sieste, G. Glaßer, I. Lieberwirth, C. Schilling, S. Fischer, H. Barth, B. Knöll, C. V. Synatschke and T. Weil, *Adv. Mater.*, 2019, **31**, 1805044.
15. Z. Sun, F. Lv, L. Cao, L. Liu, Y. Zhang and Z. Lu, Angew. Chem., *Int. Ed.*, 2015, **54**, 7944-7948 (*Angew. Chem.*, 2015, **127**, 8055-8059).
16. M. Yue, Y. Hoshino, Y. Ohshiro, K. Imamura and Y. Miura, *Angew. Chem., Int. Ed.*, 2014, **53**, 2654-2657 (*Angew. Chem.*, 2014, **126**, 2692-2695).
17. H. L. Lim, Y. Hwang, M. Kar, S. Varghese, *Biomater. Sci.*, 2014, **2**, 603-618.
18. Y. Yanga, Y. Yanga, Y. Caoa, X. Wangb, Y. Chenc, H. Liu, Y. Gaoa, J. Wang, C. Liu, W. Wang, J.-K. Yuc and D. Wub, *Chem. Eng. J.*, 2020, **403**, 126431.
19. L. Li, J. M. Scheiger, P. A. Levkin, *Adv. Mater.*, 2018, **31**, 1807333.
20. Y. Wei, Q. Zeng, M. Wang, J. Huang, X. Guo and L. Wang, *Biosens. Bioelectron.*, 2019, **131**, 156-162.
21. Y. Zhao, C.-Y. Lo, L. Ruan, C.-H. Pi, C. Kim, Y. Alsaid, I. Frenkel, R. Rico, T.-C. Tsao and X. He, *Sci. Rob.*, 2021, **6**, eabd5483.
22. J. S. Scarpa, D. D. Mueller and I. M. Klotz, *J. Am. Chem. Soc.*, 1967, **89**, 6024.

23. D. Kim, H. Kim, E. Lee, K. S. Jin and J. Yoon, *Chem. Mater.*, 2016, **28**, 8807-8814.
24. J. Hofkens, J. Hotta, K. Sasaki, H. Masuhara and K. Iwai, *Langmuir*, 1997, **13**, 414-419.
25. L. Tang, L. Wang, X. Yanga, Y. Feng, Y. Li and W. Feng, *Prog. Mater. Sci.*, 2021, **115**, 100702.
26. G. Gao, Z. Wang, D. Xu, L. Wang, T. Xu, H. Zhang, J. Chen and J. Fu, *ACS Appl. Mater. Interfaces*, 2018, **10**, 41724-41731.
27. B.-Y. Wu, X.-X. Le, Y.-K. Jian, W. Lu, Z.-Y. Yang, Z.-K. Zheng, P. The´ato, J.-W. Zhang, A. Zhang and T. Chen, *Macromol. Rapid Commun.*, 2019, **40**, 1800648.
28. X. Peng, T. Liu, C. Jiao, Y. Wu, N. Chen and H. Wang, *J. Mater. Chem. B*, 2017, **5**, 7997-8003.
29. C. Yu, Z. Duan, P. Yuan, Y. Li, Y. Su, X. Zhang, Y. Pan, L. L. Dai, R. G. Nuzzo, Y. Huang, H. Jiang and J. A. Rogers, *Adv. Mater.*, 2012, **25**, 1541-1546.
30. S. Samantaa, R. Yadavb, A. Kumara, A. K. Sinhab and R. Srivastava, *Appl. Catal., B*, 2019, **259**, 118054.
31. P. Yang, R. Wang, M. Zhou and X. Wang, *Angew. Chem., Int. Ed.*, 2014, **53**, 2654-2657 (*Angew. Chem.*, 2018, **130**, 8810-8813).
32. L.-M. Zhao, Q.-Y. Meng, X.-B. Fan, C. Ye, X.-B. Li, B. Chen, V. Ramamurthy, C.-H. Tung and L.-Z. Wu, *Angew. Chem., Int. Ed.*, 2017, **56**, 1-6 (*Angew. Chem.*, 2017, **129**, 1-6).
33. K. M. Cho, K. H. Kim, K. Park, C. Kim, S. Kim, A. Al-Saggaf, I. Gereige and H.-T. Jung, *ACS Catal.*, 2017, **7**, 7064-7069.
34. O. Erol, A. Pantula, W. Liu and D. H. Gracias, *Adv. Mater.*, 2019, **4**, 1900043.
35. Z. Jiang, L. Wang, J. Lei, Y. Liu and J. Zhang, *Appl. Catal.*, B, 2019, **241**, 367-374.